



Three-dimensional reconstruction and analysis of an entire solid oxide fuel cell by full-field transmission X-ray microscopy

J. Scott Cronin ^a, Yu-chen Karen Chen-Wiegart ^b, Jun Wang ^b, Scott A. Barnett ^{a,*}

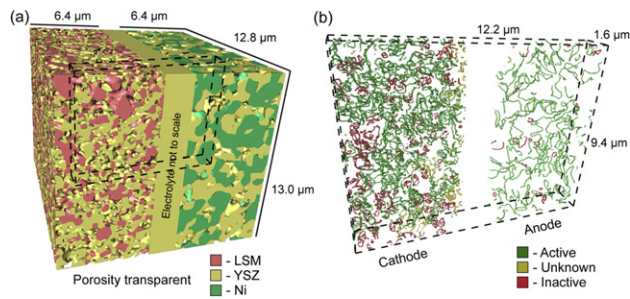
^a Department of Materials Science and Engineering, Northwestern University, Evanston, IL, USA

^b Photon Science Directorate, Brookhaven National Laboratory, Upton, NY, USA

HIGHLIGHTS

- Reconstruction of entire SOFC active region in a single set of NANO-TXM measurements.
- Cathode had 3.3× increase in TPB density due to smaller particles sizes.
- Modeled performance suggests cathode made up 85% of electrode polarization.
- LSM connectivity and sluggish TPB reaction kinetics limit cathode performance.

GRAPHICAL ABSTRACT



ARTICLE INFO

Article history:

Received 30 September 2012

Received in revised form

9 January 2013

Accepted 11 January 2013

Available online 18 January 2013

Keywords:

SOFC
Electrode
Microstructure
X-ray tomography
Reconstruction
3D

ABSTRACT

An entire active region of an anode-supported solid oxide fuel cell was structurally analyzed by X-ray computed nano-tomography using full-field transmission X-ray microscopy (NANO-TXM). A total three-dimensional volume of ~38,500 μm^3 was imaged, from which Ni–YSZ anode functional layer (~3650 μm^3) and LSM–YSZ cathode functional layer (~4100 μm^3) volumes were reconstructed. These were among the largest-volume electrode reconstructions ever reported, while at the same time exhibiting high spatial resolution of 50 nm. Comparison with electrode microstructures measured using other imaging methods demonstrates that the larger NANO-TXM-measured volumes provided significantly more accurate phase connectivity information. A microstructure-based electrochemical model prediction agreed well with the measured full-cell electrochemical data. The results suggest that low LSM connectivity and slow oxygen reduction reaction kinetics in the cathode were a major limitation to the overall cell performance.

© 2013 Elsevier B.V. All rights reserved.

1. Introduction

Solid oxide fuel cells (SOFCs) often utilize complex composite structures for both the anode and cathode. The electrode microstructure is an important factor determining its electrochemical performance, and thus the performance of the entire cell.

Quantitative 3D tomographic measurements have proved useful for understanding the relationships between microstructure, performance [1–5], and degradation [6–9]. For example, 3D data sets can be used as inputs for 3D computational models that can directly simulate electrochemical processes and microstructural evolution [10–13].

The two techniques that have been utilized for 3D tomography, FIB-SEM [14] and NANO-TXM [15], have differing advantages and disadvantages. FIB-SEM currently has a better ultimate spatial resolution, ~20 nm compared to ~40–50 nm for NANO-TXM.

* Corresponding author. Tel.: +1 847 491 2447; fax: +1 847 491 7820.

E-mail address: s-barnett@northwestern.edu (S.A. Barnett).

However, in NANO-TXM the same resolution can be maintained for relatively large measurement volumes, whereas FIB-SEM images of large volumes usually have poorer resolution. In FIB-SEM, contrast between phases is extremely sensitive to electron beam energy, detector type, and the specific phases involved, requiring considerable optimization to achieve high-contrast images. NANO-TXM is able to provide chemical contrast in cases where measurements can be done at X-ray energies above and below an elemental absorption edge, *i.e.*, X-ray absorption spectroscopy.

In this paper, a state-of-the-art Ni–YSZ||YSZ||LSM–YSZ anode-supported SOFC was fabricated, tested, and microstructurally characterized using NANO-TXM. The ability to measure large volumes with good resolution was utilized to reconstruct the entire fuel cell active region using a single set of measurements. The total measured volume was $\sim 38,500 \mu\text{m}^3$, the largest ever collected with sub 50 nm resolution (to the authors' knowledge), of which $\sim 7750 \mu\text{m}^3$ of anode and cathode volume was reconstructed and analyzed. The large volumes provided good measurement statistics, helping to minimize errors in measured structural parameters and assured that the measured data was representative of the electrodes [15]. Polarization resistances, predicted using microstructural data in a simple 1D model, were compared with the measured electrochemical test results. The differences between data collected via FIB-SEM and NANO-TXM are discussed.

2. Experimental

2.1. Sample preparation

SOFCs were prepared in an anode-supported button-cell geometry. The cell support was a $\sim 750 \mu\text{m}$ thick 60:40 wt.% NiO/YSZ pellet. A 65:35 wt.% NiO/YSZ anode functional layer and a YSZ electrolyte were colloidally deposited on the support and subsequently fired at 1400°C for 4 h, yielding a $\sim 20 \mu\text{m}$ thick dense NiO–YSZ layer and $\sim 10 \mu\text{m}$ thick dense YSZ layer. A 15 μm 50:50 wt.% LSM/YSZ composition cathode and 10 μm LSM current collector were then screen-printed and fired at 1175°C for 1 h. Further details of the processing have been reported elsewhere [15]. Fuel cells were sealed with silver ink on alumina tubes. During testing, humidified hydrogen was supplied on the inside of the tube to the anode, while the cathode side of the cell was exposed to laboratory air.

For post-performance structural analysis, a cylindrical sample with a diameter of $\sim 35 \mu\text{m}$ and height of $\sim 80 \mu\text{m}$ was milled from the SOFC using a focused ion beam. This cylinder was mounted onto a tungsten pin using a lift-out technique [15]. The cylindrical sample, which contained all three layers – anode, electrolyte and cathode – of SOFC structure was then examined by X-ray nano-tomography.

2.2. Electrochemical characterization

Electrochemical impedance spectroscopy (EIS) testing was completed at 800°C prior to any electrode polarization. A Zahner IM6 electrochemical workstation was utilized to collect impedance spectra from a 100 mHz to 1 MHz frequency range, at open circuit voltage (OCV). Additionally, current–voltage characteristics were measured at 10 mV increments from OCV to 0 V. The cell was then operated at 2.6 A cm^{-2} at 800°C in air and humidified hydrogen for 16 h to allow for electrode break in. The EIS measurements were repeated after cell discharge.

2.3. NANO-TXM characterization

The nano-tomography experiments were carried out at the transmission X-ray microscopy (NANO-TXM) beamline X8C, National Synchrotron Light Source, Brookhaven National Laboratory

[16]. NANO-TXM is a full-field imaging technique, which currently provides a sub-30 nm 2D resolution with tomography capability. Four tomography data sets were collected from the same SOFC sample with different X-ray energies – below and above the Ni K-edge (at 8300 and 8400 eV) and Mn K-edge (at 6500 and 6600 eV) – to facilitate the segmentation process. Each tomography measurement consisted of 1441 projections over a 180° angular range with 40 μm field of view and 50 nm spatial resolution. The alignment of the X-ray projections was performed automatically using a passive rotational run-out correction system [16]. A standard filtered backprojection reconstruction algorithm was used to reconstruct the 3D structure, and extract a stack of virtual cross-section slices from each tomography dataset [17]. The voxel size of the reconstructed volume is 38.9 nm after 2 by 2 pixel binning.

2.4. Image processing

Prior to segmentation, the sets of electrode cross-sectional slices were cropped. For the Ni–YSZ anode, three different volumes were extracted to maximize the information analyzed. The volumes were selected to avoid specific artifacts in the dataset that could compromise the integrity of the reconstruction. For the LSM–YSZ cathode, a single large dataset was extracted as no artifacts were present. The images collected below and above the K adsorption edge of Ni were used to segment the anode. The two data sets were first registered in 3D space and segmented by thresholding. Details of this process are given elsewhere [15].

For the cathode region, the data collected below and above the Mn edge did not show significant contrast difference, mainly because Mn constitutes only 20% of atoms in the LSM phase. The cathode segmentation was thus performed using only the above-Mn-edge data that provided better contrast between LSM and the other two phases. Furthermore, thresholding did not yield accurate segmentation because of the small feature size and limited contrast, leading to many single voxel errors. Therefore, to segment the LSM, YSZ, and pore phases, a watershed algorithm with 2D histogram seeding was used with commercial software (Avizo VSG, version 6.2) [18,19]. In this procedure, a 2D histogram is calculated from the reconstructed slices, providing a distribution map of the grayscale gradient versus the grayscale value from each individual voxel. Three distinct clusters with low grayscale gradient were identified from the 2D histogram and used as the seeding voxels. Low gradient voxels are found in the internal particle regions for each of the three phases and thus can be accurately identified. On the contrary, the voxels with high gradients are near the interfaces between two or three phases and are not identified at this stage. A region-growing method was then applied to assign these unknown voxels to their respective phases [20]. The results of the segmentation are checked with similar cathodes reconstructed using threshold segmentation of FIB-SEM data [1,2], and demonstrate similar quantitative results ensuring high fidelity in the segmentation process; a comparison is discussed in more detail later.

2.5. Microstructural quantification

Macrohomogenous morphological information including phase volume fraction, surface areas, phase size distributions, phase connectivity, triple phase boundaries (TPBs), and tortuosity was calculated. Algorithms were written to calculate these parameters in several image processing programs including Interactive Data Language (IDL), and Matlab as described elsewhere [1,2,6,15]. The tortuosity was calculated using an ImageJ plug-in developed by Maire et al. [21].

Phase intra-connectivity was analyzed for all three phases of each composite electrode. A directional method was implemented

in which ‘connected’ phases of the electronic conductor and porosity were required to connect to the current collector, while the ionic conductor was required to connect to the electrolyte [6,22]. A network was labeled ‘isolated’ if it did not connect to any side of the reconstruction. Finally, the remainder – networks that appeared isolated but intersected an edge of the measured volume such that their true connectivity was indeterminate – was labeled ‘unknown’.

The electrochemically-active component of the TPB density was determined with the aid of the phase intra-connectivity information. Only TPBs lying on the intersection of ‘connected’ electronic conductor, ionic conductor, and pore phases were considered to be electrochemically active. If any of the phases were ‘isolated’, the TPB was categorized as ‘inactive’. Furthermore, if one or more phases were labeled ‘unknown’, with the others connected, the TPB on that particle was also ‘unknown’. In order to determine the true electrochemically-active TPB density, the unknown portion was then mathematically split into ‘active’ and ‘inactive’ amounts via a proportion consistent to the measured active and inactive TPB fractions [1].

2.6. Error analysis

The fraction of unknown TPBs was relatively small at 2.6% for the anode and 10% for the cathode, because of the relatively large NANO-TXM reconstruction volumes. Associated errors were thus quite small.

The large-volume ($\sim 4000 \mu\text{m}^3$) data sets analyzed in this work were substantially larger than in most prior NANO-TXM reports ($\sim 14\text{--}680 \mu\text{m}^3$) [19,22–24], and also larger than most FIB-SEM data sets ($\sim 530\text{--}1400 \mu\text{m}^3$) [1,2,6]. The key advantage here is for ensuring that the volume analyzed is representative and that macrohomogenous parameters obtained are accurate. Prior work suggests that a principle axis length in a cubic reconstruction should be ≥ 16 times the average particle size, in order to achieve reasonable ($<3\%$ error) statistics in the values extracted [25]. In the present case, the anode had an average coordinate length to average Ni particle size ratio of ~ 18.4 ; the YSZ and pore phase feature sizes were nearly a factor of two smaller and hence had much larger ratios. The cathode was even greater with an average coordinate length to average LSM particle size ratio of ~ 49 (LSM had the largest average size in the cathode). These ratios are well above a required volume needed and ensure that the measured values are accurate.

The present measurement with a voxel size of 38.9 nm for a large ($40 \mu\text{m}$) field of view, was typical of resolution observed in other NANO-TXM studies, and slightly worse than data obtained with FIB-SEM 3D tomography, typically 20–40 nm [1,6,26]. For the present case, this yields ratios of the average YSZ particle size to resolution of 17 for the anode and 10 for the cathode; values for YSZ are quoted here since they had the smallest average size. Prior studies have shown that a ratio of the average particle size to resolution of 15 is needed for error $<5\%$, while a ratio of 10 can yield up to 8% error [25]. The present anode results should thus have good accuracy with slightly worse accuracy for the cathode. Note that LSM, Ni, and pore average sizes were larger than for YSZ, such that their associated measurement accuracies were better. For example, the LSM and pore ratios in the cathode were 13.5 and 16.3 – this reduces overall cathode error since these phases made up 74% of the electrode volume.

3. Results

3.1. Structural quantification

The anode functional layer (AFL) and cathode functional layer (CFL) structures were analyzed separately. For the anode, three

volumes of approximately $\sim 1200 \mu\text{m}^3$ were analyzed and the structural parameters were averaged using volume as a weighting factor. The AFL composition was 65:35 wt.% NiO/YSZ and was sintered to nearly 100% density, such that the porosity resulted from NiO to Ni reduction upon anode exposure to fuel, allowing theoretical volume fractions to be determined for all three phases. Theoretical volume fraction calculations, assuming the NiO–YSZ composite was 100% dense prior to reduction, yield 36.6% Ni, 37.8% YSZ, and 25.6% porosity. The experimental values are listed in Table 1 and show good agreement with these theoretical values.

Unlike the AFL, the CFL was analyzed as a single very large $\sim 4100 \mu\text{m}^3$ dataset. Because the cathode was not fired dense, an *a priori* value for the volume fraction of porosity was not available. However, the LSM-to-YSZ volume ratio is known to be 47.6:52.4 vol.%, given that the starting cathode was made with 50 wt.% LSM and 50 wt.% YSZ. The measured volume fractions listed in Table 1 show a volume ratio 46.8:53.2, also in good agreement with expected values. These volume fractions, including the pore volume, also match well with previous FIB-SEM measurements on similarly processed cathodes [1,2,27]. The cathode pore volume fraction is large relative to the anode due to the lower firing temperature of the cathode (1175 °C versus the 1400 °C for the anode), such that the cathode structure was not fully sintered.

A full reconstruction of the volume analyzed can be seen in Fig. 1(a) with the cathode on the left and anode on the right. The electrolyte region is shown for visualization purposes, and is not to scale. One clearly apparent difference between the electrodes is the larger particle size in the anode. Fig. 2 shows the effective feature size distributions of each phase [28]. A general observation is that particles in the cathode are smaller and have less dispersion in size when compared to phases in the anode, especially the Ni phase.

Table 1 lists the measured surface areas for specific phases, broken down both as total area and interfacial area between each pair of phases. It is important to note that the specific surface area is normalized by the volume of the specified phase, while the interfacial surface area is normalized by the volume of the reconstruction itself. The pore surface area is relatively large and similar for both electrodes. However, the surface areas for the cathode YSZ and LSM phases are much greater than the anode YSZ and Ni phases, consistent with the particle size results. Noting that the YSZ starting powder was the same for cathode and anode, it is clear that

Table 1
Measured 3D structural parameters for the composite anode and cathode.

| Anode | Cathode |
|---|---------|
| <i>Volume analyzed (μm^3)</i> | |
| Anode | 3641 |
| <i>Phase volume fractions (%)</i> | |
| Ni | 36.9 |
| YSZ | 40.1 |
| Pore | 23.0 |
| <i>Specific surface area ($\mu\text{m}^2/\mu\text{m}^3$)</i> | |
| Ni | 4.11 |
| YSZ | 6.01 |
| Pore | 7.56 |
| <i>Interfacial areas ($\mu\text{m}^2/\mu\text{m}^3$)</i> | |
| Ni–YSZ | 1.09 |
| YSZ–pore | 1.31 |
| Ni–pore | 0.42 |
| <i>Volume fraction connected (%)</i> | |
| Ni | 99.3 |
| YSZ | 100.0 |
| Pore | 98.8 |
| <i>TPB density ($\mu\text{m}/\mu\text{m}^3$)</i> | |
| Total | 3.06 |
| Active | 2.89 |
| Inactive | 0.17 |
| <i>Total</i> | |
| Active | 10.24 |
| Inactive | 6.73 |
| | 3.51 |

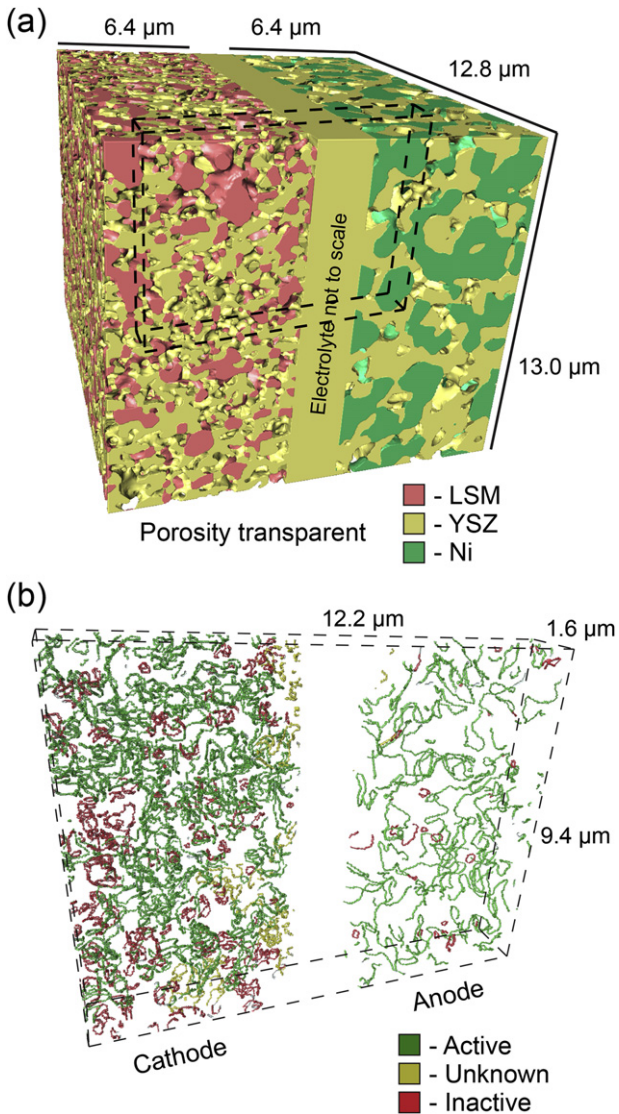


Fig. 1. 3D reconstruction images showing (a) solid phases and (b) TPB lines in a SOFC structure, with the cathode on the left and anode on the right. The anode volume shown is one of the three separate measured volumes; the much larger measured cathode volume was cropped to match the anode dimensions. The image orientations in (a) and (b) are the same, but the TPB view in (b) shows a thinner region cropped from the full volume, for clarity. The electrolyte is shown only as a visualization aid – the image does not indicate its true thickness or the structure of the interfaces.

these differences relate mainly to the lower cathode firing temperature, which yielded less particle coarsening/sintering than in the anode during processing. In the anode, there is relatively little Ni–pore interface. Indeed, most of the Ni interface is with YSZ versus pore; this lack of Ni–pore interfaces may limit Ni coarsening and associated performance reductions [6]. On the other hand, most interfacial area in the cathode stems from the pore phase and is most significant for the YSZ–pore interface. This difference is likely due to the fact that the cathode was fired at a lower temperature leading to higher total pore volume and surface area.

Connectivity was also analyzed for each phase. The anode had each phase nearly 100% connected in the direction required for the electrochemical reactions. For the cathode, the YSZ and pore phases were fully connected, but the LSM phase was 76% connected, 14% isolated, and 10% unknown. This can be explained by the relatively low LSM volume fraction and the presence of some larger particles

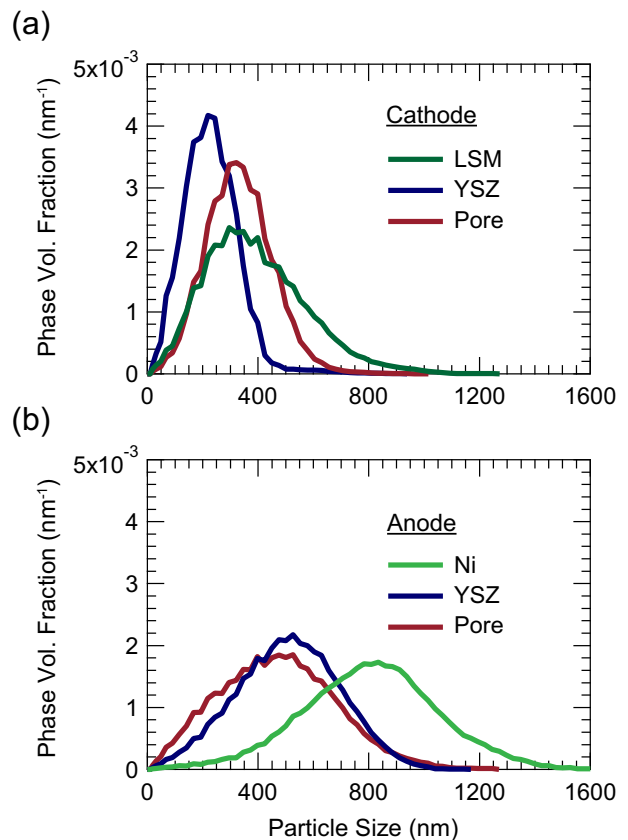


Fig. 2. Particle size distribution for cathode composite phases (a) and anode composite phases (b). The magnitude of the y-axis is normalized such that the sum of all fractions for a given phase = 1 rather than the overall volume fraction listed in Table 1.

(Fig. 2), which limits the probability of forming connected pathways to the current collector.

The total TPB density was 3.3 times larger for the cathode than the anode, though the active component was only 2.3 times larger. The reduction in the active TPB ratio was a direct result of the low LSM connected fraction. This is readily seen in Fig. 1(b), which shows the higher total TPB density in the cathode, but with a substantial fraction of inactive TPB lines (indicated in red). The region shown was extracted from the center of the dataset, allowing better visualization of the TPBs while simultaneously eliminating unknown TPBs which form near the edges of the reconstruction (For interpretation of the references to colour in this paragraph, the reader is referred to the web version of this article.).

The tortuosities of the YSZ phases in the anode and cathode were determined to be 1.26 and 1.51, respectively. This is relevant to performance because the effective ionic conductivity in the electrode is inversely proportional to the YSZ tortuosity factor (the square of the tortuosity) [1,2]. The tortuosities of the porosity and electronic conductor in the AFL or CFL were not computed since they are unlikely to affect performance: concentration polarization is minimal in 15–20 μm thick electrodes and electronic conductivities are orders of magnitude larger than ionic conductivities such that electronic resistance is insignificant.

3.2. Electrochemical performance analysis

The electrochemical data, taken after cell operation for 16 h, is shown in Fig. 3. From the Nyquist plot in Fig. 3(a), the ohmic resistance was 0.05 Ω cm² and total electrode polarization resistance was 0.30 Ω cm². Fig. 3(b) shows that there were two main

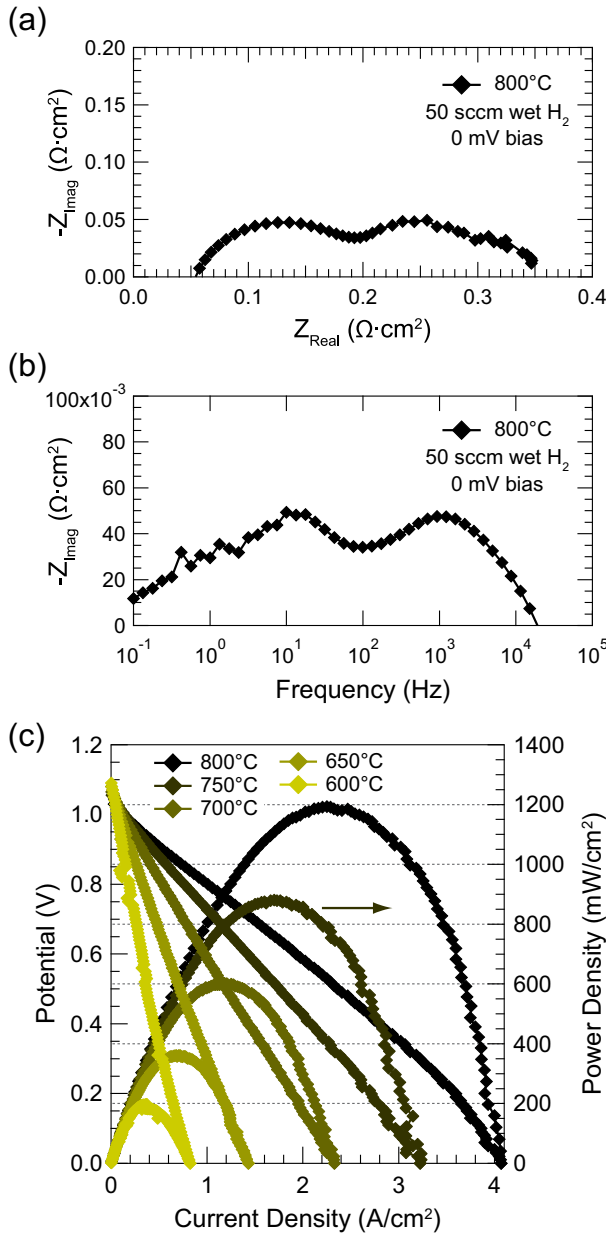


Fig. 3. Nyquist (a) and Bode (b) plots of the EIS data taken at 800 °C at open circuit potential after SOFC operation for 16 h. Potential and power density plots versus current density for different temperatures (c). All measurements were taken with humidified hydrogen at the anode and laboratory air at the cathode.

impedance responses, centered at ~ 10 and ~ 1000 Hz. The open circuit voltage at 800 °C was 1045 mV, slightly below the theoretical value for these conditions, but normal for this test configuration where there was slight seal leakage [29]. The current–voltage curves were mostly linear, with a slight indication of concentration polarization at the highest current density, likely stemming from the thick anode support. The power density at 800 °C and 0.7 V was 1.04 W cm^{-2} .

3.3. Electrochemical modeling

The macrohomogenous structural information obtained above was input into a simple one-dimensional model [30] to predict each electrode's area-specific polarization resistance. The model geometrically replicates the structure of an electrode by extending

ionic-conducting columns from the electrolyte into the electrode; the column surface resistance was obtained by distributing the measured active TPB density on the columns and applying literature values of TPB line resistance [2,31,32]. Model assumptions as well as the inputs from structural information are listed explicitly in Table 2. The model predicts an anode polarization resistance of $0.043 \Omega \text{ cm}^2$ and a cathode polarization resistance of $0.25 \Omega \text{ cm}^2$. The sum of the two components, $0.29 \Omega \text{ cm}^2$ is in remarkably good agreement with the measured cell polarization resistance (Fig. 3(a)) of $0.30 \Omega \text{ cm}^2$. Note that no fitting parameters were used in the calculation.

4. Discussion

The measured anode and cathode structural parameters listed in Table 1 and Fig. 2 are in good agreement with previously reported FIB-SEM 3D tomographic data for similarly processed SOFCs [1,2,6]. Specifically, the anode values were consistent with prior specific surface areas ($\text{Ni} = 5.66 \mu\text{m}^{-1}$, $\text{YSZ} = 4.83 \mu\text{m}^{-1}$, pore = $9.76 \mu\text{m}^{-1}$), interfacial areas ($\text{Ni}-\text{YSZ} = 1.21 \mu\text{m}^{-1}$, $\text{Ni}-\text{pore} = 0.36 \mu\text{m}^{-1}$, and $\text{YSZ}-\text{pore} = 1.40 \mu\text{m}^{-1}$), and TPB densities (total TPB = $3.37 \mu\text{m}^{-2}$), although the Ni content was slightly lower in this prior report (the starting NiO/YSZ weight ratio was 50:50 versus the present 65:35 composition) [6]. This difference likely explains slight differences in the results, especially higher porosity connectivity of the present anodes than in the prior low-Ni-content anodes, which led to a higher percentage of active TPBs.

A nearly identical cathode analyzed by FIB-SEM [1] yielded similar quantities – the specific surface areas ($\text{LSM} = 10.7 \mu\text{m}^{-1}$, $\text{YSZ} = 17.2 \mu\text{m}^{-1}$, pore = $9.7 \mu\text{m}^{-1}$) and TPB density ($15.9 \mu\text{m}^{-2}$) were slightly higher in the FIB-SEM data, suggesting a slight underestimation of these values perhaps due to the lower NANO-TXM resolution. One useful result of the larger volume measured in the present data is improved accuracy of phase intra-connectivity, and hence active TPB densities. The FIB-SEM study yielded a higher fraction (20%) of unknown LSM (with 67% connected and 13% isolated), twice the value in the present study.

Results of the microstructural modeling demonstrate that the cathode made up 85% of the total electrode polarization resistance. The cathode prediction was then modified to include the total TPB density as opposed to just the active TPB density. With all other inputs being equal, and a total TPB density of $10.24 \mu\text{m}^{-2}$, the expected resistance decreased by 26%, resulting in a cathode polarization of $0.187 \Omega \text{ cm}^2$ and a total cell polarization of $0.230 \Omega \text{ cm}^2$. Taking into account the ohmic resistance from the thin electrolyte,

Table 2

Key values used in a one dimensional microstructure-based model and the resulting electrode polarization resistance predictions.

| Assumptions for TFV model | | |
|--|---|---------|
| YSZ conductivity (800 °C) | 0.055 S cm^{-1} | |
| Anode TPB line resistivity (800 °C) | $8.29 \times 10^3 \Omega \text{ cm}$ [31] | |
| Cathode TPB line resistivity (800 °C) | $1.9 \times 10^5 \Omega \text{ cm}$ [2] | |
| Microstructural inputs for TFV model | | |
| Electrode thickness (μm) | Anode | Cathode |
| YSZ volume fraction | 20 | 15 |
| Average YSZ particle size (nm) | 0.401 | 0.263 |
| YSZ tortuosity factor | 526 | 244 |
| Active TPB density (μm^{-2}) | 1.59 | 2.28 |
| TFV model predictions | | |
| $R_{\text{Pol-Anode}}$ | $0.043 \Omega \text{ cm}^2$ | |
| $R_{\text{Pol-Cathode}}$ | $0.252 \Omega \text{ cm}^2$ | |
| $R_{\text{Pol-Total}}$ | $0.295 \Omega \text{ cm}^2$ | |
| Experimental electrode polarization resistance | | |
| $R_{\text{Pol-Total}}$ | $0.30 \Omega \text{ cm}^2$ | |

it is calculated that the power density would improve by ~19%. In order to achieve these results, all inactive TPBs would need to be converted to active TPBs by modifying the cathode processing. Unfortunately, increasing LSM content did not lead to higher performance since the improvement in LSM connectivity was balanced by changes in the total TPB density and YSZ tortuosity [2]. However, other methods to increase connectivity without affecting these properties could allow significant performance improvements to be realized.

Similarly, a calculation was completed to determine the amount of active TPB in the cathode required to match the polarization resistance of the anode. A 19× increase in active TPB for the current cathode was required, stemming from the fact that the TPB line resistivity is much lower for the cathode than the anode.

5. Conclusions

NANO-TXM was used to reconstruct a solid oxide fuel cell active region with 38,500 μm^3 volume in a single set of measurements. X-ray energies were tuned above and below the Ni K-edge to enhance contrast needed for segmenting the anode solid phases, while cathode segmentation relied on segmentation of data above the Mn edge. The unprecedented large volumes measured combined with good resolution yielded surface areas, network connectivities, and TPB densities with very good accuracy. The cathode generally had smaller average particle sizes than the anode, leading to higher TPB densities. The active component of cathode TPB density was decreased by the significant fraction of isolated LSM particles, while the anode TPB density was nearly all active. The electrode polarization resistance calculated based on microstructural inputs was 0.29 $\Omega \text{ cm}^2$, in good agreement with the EIS-measured value of 0.30 $\Omega \text{ cm}^2$. The cathode made up nearly 85% of the cell polarization resistance, despite its higher TPB density. Thus, microstructural engineering to increase the cathode active TPB density should be effective for improving overall cell performance.

Acknowledgments

The authors gratefully acknowledge the financial support from the National Science Foundation Ceramics program through grant DMR-0907639. Furthermore, efforts by Kyle Yakal-Kremski for electrode visualization and Prof. Eric Maire who provided us with the ImageJ plug-in for tortuosity calculations are greatly appreciated. We thank Dr. Fernando Camino (BNL) for assisting the development of the sample preparation procedure using FIB/SEM at the Center for Functional Nanomaterials, Brookhaven National Laboratory, which is supported by the U.S. Department of Energy, Office of Basic Energy Sciences, under Contract No. DE-AC02-98CH10886. Use of the National Synchrotron Light Source, Brookhaven National Laboratory, was supported by the U.S. Department

of Energy, Office of Science, Office of Basic Energy Sciences, under Contract No. DE-AC02-98CH10886.

References

- [1] J.S. Cronin, K. Muangnapoh, Z. Patterson, K.J. Yakal-Kremski, V.P. Dravid, S.A. Barnett, *J. Electrochem. Soc.* 159 (2012) B385–B393.
- [2] J.R. Wilson, J.S. Cronin, A.T. Duong, S. Rukes, H.-Y. Chen, K. Thornton, D.R. Mumm, S. Barnett, *J. Power Sources* 195 (2010) 1829–1840.
- [3] J.R. Wilson, J.S. Cronin, S.A. Barnett, *Scripta Mater.* 65 (2011) 67–72.
- [4] A.T. Duong, D.R. Mumm, *J. Electrochem. Soc.* 159 (2012) B40–B53.
- [5] L. Holzer, B. Münch, B. Iwanschitz, M. Cantoni, T. Hocker, T. Graule, *J. Power Sources* 196 (2011) 7076–7089.
- [6] J.S. Cronin, J.R. Wilson, S.A. Barnett, *J. Power Sources* 196 (2011) 2640–2643.
- [7] Z. Jiao, N. Shikazono, N. Kasagi, *J. Electrochem. Soc.* 159 (2012) B285–B291.
- [8] H. Sumi, R. Kishida, J.-Y. Kim, H. Muroyama, T. Matsui, K. Eguchi, *J. Electrochem. Soc.* 157 (2010) B1747–B1752.
- [9] L. Holzer, B. Iwanschitz, T. Hocker, B. Münch, M. Prestat, D. Wiedenmann, U. Vogt, P. Holtappels, J. Sfeir, A. Mai, T. Graule, *J. Power Sources* 196 (2011) 1279–1294.
- [10] H.-Y. Chen, H.-C. Yu, J. Scott Cronin, J.R. Wilson, S.A. Barnett, K. Thornton, *J. Power Sources* 196 (2011) 1333–1337.
- [11] D. Kanno, N. Shikazono, N. Takagi, K. Matsuzaki, N. Kasagi, *Electrochim. Acta* 56 (2011) 4015–4021.
- [12] M. Kishimoto, H. Iwai, M. Saito, H. Yoshida, *J. Power Sources* 196 (2011) 4555–4563.
- [13] U. Doraswami, P. Shearing, N. Droushiotis, K. Li, N.P. Brandon, G.H. Kelsall, *Solid State Ionics* 192 (2011) 494–500.
- [14] J.R. Wilson, W. Kobsiriphat, R. Mendoza, H.Y. Chen, J.M. Hiller, D.J. Miller, K. Thornton, P.W. Voorhees, S.B. Adler, S.A. Barnett, *Nat. Mater.* 5 (2006) 541–544.
- [15] Y.-C.K. Chen-Wiegert, J.S. Cronin, Q. Yuan, K.J. Yakal-Kremski, S.A. Barnett, J. Wang, *J. Power Sources* 218 (2012) 348–351.
- [16] J. Wang, Y.-C.K. Chen, Q. Yuan, A. Tkachuk, C. Erdonmez, B. Hornberger, M. Feser, *Appl. Phys. Lett.* 100 (2012). 143107–143104.
- [17] F. Natterer, *The Mathematics of Computerized Tomography*, Society for Industrial and Applied Mathematics, 2001.
- [18] D. Marinha, L. Dessemond, J.S. Cronin, J.R. Wilson, S.A. Barnett, E. Djurado, *Chem. Mater.* 23 (2011) 5340–5348.
- [19] P.R. Shearing, R.S. Bradley, J. Gelb, S.N. Lee, A. Atkinson, P.J. Withers, N.P. Brandon, *Electrochem. Solid-State Lett.* 14 (2011) B117–B120.
- [20] R. Azriel, C.K. Avinash, *Digital Picture Processing*, second ed., Academic Press, Inc., 1982.
- [21] E. Maire, O. Caty, A. King, J. Adrien, in: *IUTAM Symposium on Mechanical Properties of Cellular Materials*, 2009, pp. 35–42.
- [22] P.R. Shearing, J. Gelb, J. Yi, W.K. Lee, M. Drakopoulous, N.P. Brandon, *Electrochem. Commun.* 12 (2010) 1021–1024.
- [23] K.N. Grew, Y.S. Chu, J. Yi, A.A. Peracchio, J.J.R. Izzo, Y. Hwu, F. De Carlo, W.K.S. Chiu, *J. Electrochem. Soc.* 157 (2010) B783–B792.
- [24] G.J. Nelson, W.M. Harris, J.J. Lombardo, J.R. Izzo Jr., W.K.S. Chiu, P. Tanasini, M. Cantoni, J. Vanherle, C. Comninellis, J.C. Andrews, Y. Liu, P. Pianetta, Y.S. Chu, *Electrochem. Commun.* 13 (2011) 586–589.
- [25] J.S. Cronin, Ph.D. Thesis, Department of Materials Science and Engineering, Northwestern University, Evanston, IL, 2012, pp. 1–245.
- [26] H. Iwai, N. Shikazono, T. Matsui, H. Teshima, M. Kishimoto, R. Kishida, D. Hayashi, K. Matsuzaki, D. Kanno, M. Saito, H. Muroyama, K. Eguchi, N. Kasagi, H. Yoshida, *J. Power Sources* 195 (2009) 955–961.
- [27] J.R. Wilson, S.A. Barnett, *Electrochem. Solid-State Lett.* 11 (2008) B181–B185.
- [28] B. Münch, L. Holzer, *J. Am. Ceram. Soc.* 91 (2008) 4059–4067.
- [29] P. Von Dollen, S. Barnett, *J. Am. Ceram. Soc.* 88 (2005) 3361–3368.
- [30] C.W. Tanner, K.Z. Fung, A.V. Virkar, *J. Electrochem. Soc.* 144 (1997) 21–30.
- [31] W.G. Bessler, M. Vogler, H. Stormer, D. Gerthsen, A. Utz, A. Weber, E. Ivers-Tiffee, *Phys. Chem. Chem. Phys.* 12 (2010) 13888–13903.
- [32] R. Radhakrishnan, A.V. Virkar, S.C. Singhal, *J. Electrochem. Soc.* 152 (2005) A210.